Opto-Electronic Advances

CN 51–1781/TN ISSN 2096–4579 (Print) ISSN 2097–3993 (Online)

High-resolution tumor marker detection based on microwave photonics demodulated dual wavelength fiber laser sensor

Jie Hu, Weihao Lin, Liyang Shao, Chenlong Xue, Fang Zhao, Dongrui Xiao, Yang Ran, Yue Meng, Panpan He, Zhiguang Yu, Jinna Chen and Perry Ping Shum

Citation: Hu J, Lin WH, Shao LY, et al. High-resolution tumor marker detection based on microwave photonics demodulated dual wavelength fiber laser sensor. *Opto-Electron Adv* **7**, 240105(2024).

https://doi.org/10.29026/oea.2024.240105

Received: 18 July 2024; Accepted: 13 September 2024; Published online: 16 December 2024

Opto-Electronic Advances

Article

December 2024, Vol. 7, No. 12

DOI: 10.29026/oea.2024.240105 CSTR: 32247.14.oea.2024.240105

High-resolution tumor marker detection based on microwave photonics demodulated dual wavelength fiber laser sensor

Jie Hu[1], Weihao Lin[1], Liyang Shao[1]*, Chenlong Xue[1], Fang Zhao[1], Dongrui Xiao[2]*, Yang Ran[3], Yue Meng[4], Panpan He[5], Zhiguang Yu[5], Jinna Chen[1] and Perry Ping Shum[1]

The specific detection of tumor markers is crucial in early tumor screening and subsequent treatment processes. To accurately distinguish the signal response caused by trace markers, the high demodulation resolution of the sensor is necessary. In this paper, we propose a dual-wavelength fiber laser sensing system enhanced with microwave photonics demodulation technology to achieve high-resolution tumor marker detection. This sensing system can simultaneously perform spectral wavelength-domain and frequency-domain analyses. Experimental results demonstrate that this system's refractive index (RI) sensitivity reaches 1083 nm/RIU by wavelength analysis and –1902 GHz/RIU by frequency analysis, with ideal detection resolutions of 1.85×10^{-5} RIU and 5.26×10^{-8} RIU, respectively. Compared with traditional wavelength domain analysis, the demodulation resolution is improved by three orders of magnitude, based on the same sensing structure. To validate its biosensing performance, carcinoembryonic antigen-related cell adhesion molecule 5 (CEACAM5) is selected as the detection target. Experimental results show that the improved sensing system has a limit of detection (LOD) of 0.076 ng/mL and a detection resolution of 0.008 ng/mL. Experimental results obtained from human serum samples are consistent with clinical data, highlighting the strong clinical application potential of the proposed sensing system and analysis method.

Keywords: optical fiber sensor; optical fiber laser; microwave photonics demodulation; high-resolution detection; tumor marker detection

Hu J, Lin WH, Shao LY et al. High-resolution tumor marker detection based on microwave photonics demodulated dual wavelength fiber laser sensor. *Opto-Electron Adv* **7**, 240105 (2024).

Introduction

In recent years, cancer incidence and mortality rates have continued to rise worldwide[1]. Early-stage detection, diagnosis, and treatment are of great significance to improve the survival rate of cancer patients[2]. As a supplement to traditional diagnostic methods such as imaging examination, the detection of tumor markers has important auxiliary diagnostic value in the early screening of

[1]Department of Electronic and Electrical Engineering, Southern University of Science and Technology, Shenzhen 518055, China; [2]School of Electrical Information Engineering, Hunan Institute of Technology, Hengyang 421002, China; [3]Guangdong Provincial Key Laboratory of Optical Fiber Sensing and Communications, Institute of Photonics Technology, Jinan University, Guangzhou 510632, China; [4]Department of Clinical Laboratory, Guangdong Provincial People's Hospital, Guangdong Academy of Medical Sciences, Guangzhou 511436, China; [5]Medcaptain Medical Technology Co., Ltd., Shenzhen 518055, China.

*Correspondence: LY Shao, E-mail: shaoly@sustech.edu.cn; DR Xiao, E-mail: 11849550@mail.sustech.edu.cn

Received: 18 July 2024; Accepted: 13 September 2024; Published online: 16 December 2024

tumors[3,4]. Immunoassays such as enzyme-linked immunosorbent assay (ELISA) are prevalent in current clinical diagnosis, realizing the quantification detection of specific tumor markers, and exhibiting satisfactory sensitivity and specificity[5,6]. Nevertheless, these assays are relatively time-intensive and often necessitate skilled researchers to execute them due to their complicated sample labeling procedures. With the advent of Point-of-Care Testing (POCT) and the emergence of novel label-free detection technologies, such as those based on nanomaterials, optics, and electrochemistry, new avenues have opened for tumor marker detection[7–10]. These methods offer real-time affinity responses and rapid results while being easy to operate.

Optical fiber biosensors, which are built on silica fibers with a diameter of several hundred microns, have the characteristics of fast response, small size, low cost, and anti-electromagnetic interference. In recent years, the research of biosensors based on optical fiber has gradually emerged[11]. For example, a fiber light-coupled optofluidic waveguide biosensor was proposed for the detection of p53 protein[12]. A plasmonic optical fiber biosensor based on tilted fiber Bragg grating was proposed to detect breast cancer cells[13]. The sensitivity of the sensor can be greatly improved by attaching two-dimensional materials, metal micro-nano particles, and deposited films to the surface of the optical fiber sensor to achieve local electromagnetic field enhancement[14–16]. The antigen sandwich method based on immunoassay provides an effective strategy to amplify the signal caused by biomolecular binding events[17–19]. Several fiber laser biosensors are designed and make the change of the spectral signal more easily distinguishable[20,21]. However, a conventional optical fiber sensor is usually implemented based on wavelength monitoring using an optical spectrum analyzer (OSA), the best wavelength resolution of which is 0.02 nm. This means that when using OSA to analyze spectral wavelength changes, only the GHz order and larger frequency changes can be resolved, which restricts the sensing resolution of optical fiber sensors.

To distinguish the weak signal caused by trace tumor markers, it is necessary to employ ultrahigh-resolution interrogation methods. Microwave photonics is an interdisciplinary subject combining microwave engineering and optoelectronics[22,23]. It has potential applications in high-precision sensing systems, in which converting optical wavelength changes into microwave spectrum changes and significantly improving resolution[24,25]. Despite this, there has been little research on microwave photonics technology combined with fiber optic sensors for biological detection and even tumor marker detection. In this paper, a dual-wavelength laser sensing system assisted by microwave photonics demodulation technology is constructed for the specific detection of tumor markers in serum and demonstrated to be with high sensing resolution. The laser spectral wavelength analysis based on OSA, and the radiofrequency (RF) signal analysis based on microwave photonics demodulation are performed simultaneously and the detection performance is compared in detail. Compared with optical wavelength-based demodulation, time-delay dispersion-based microwave photonics demodulation improves the detection resolution and limit of detection (LOD) effectively. The proposed biosensor and corresponding demodulation device can be extended to a wider range of biological detection applications.

Sensor design and principle

Experimental setup

Figure 1 shows the dual-wavelength fiber laser sensor and its signal analysis system, where the laser spectral wavelength analysis based on OSA and RF signal analysis based on microwave photonics demodulation can be carried out simultaneously. As shown in the left portion of Fig. 1, a fiber ring laser cavity is constructed to achieve dual-wavelength laser output. The 980 nm pump light is injected into the fiber ring cavity through a 980/1550 wavelength division multiplexer (WDM), exciting the erbium ions in the approximately 40 cm long erbium-doped fiber (EDF) and generating signal light at approximately 1525–1565 nm. Subsequently, add an optical isolator (ISO) to ensure one-way transmission of light in the loop cavity. After passing through the ISO, the signal light is split into two paths, Path 1 and Path 2, by a 50/50 fiber optical coupler (OC1). These two paths are equipped with independent filtering structures to achieve tunability of the dual-wavelength laser. Path 1 employs a tapered lasso-shaped fiber sensor for filtering, which is described in detail below. In Path 2, filtering is achieved using a fiber Bragg grating (FBG). The signal light inside the cavity is directed into the FBG through a circulator, and the reflected light from the FBG is received back into the optical path. To balance the optical power in the two paths, an adjustable optical attenuator (OA) is included in Path 2. The filtered signal lights are then

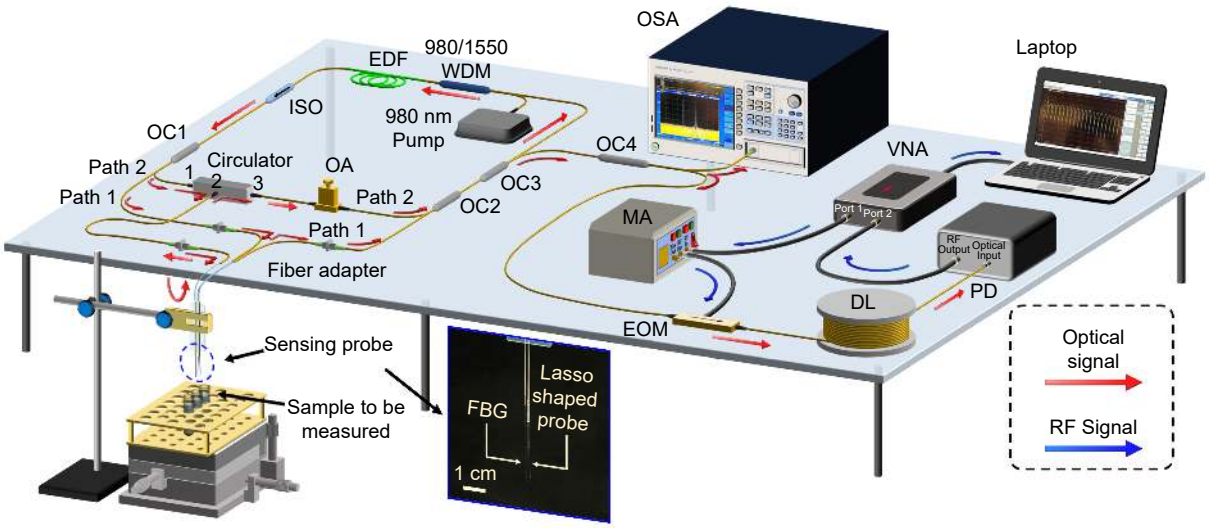

Fig. 1 | Dual-wavelength fiber laser sensor and its signal demodulation system.

merged again through a 50/50 fiber optical coupler (OC2). Finally, through a 90/10 fiber optical coupler (OC3), 10% of the signal light is output for analysis, while the remaining 90% continues to circulate and amplify within the cavity, forming the laser.

The generated laser signal is split again into two by a subsequent 50/50 fiber optical coupler (OC4), with one signal transmitted to an OSA for laser spectral analysis, and the other used for microwave photonic demodulation. In the microwave photonic demodulation scheme, as shown in the right portion of Fig. 1, the dual-wavelength laser is first input into an electro-optic modulator (EOM, iXblue, MXAN-LN-40), which is driven by a 5 V bias voltage. Meanwhile, the RF signal output (9 kHz ~ 9 GHz) from Port 1 of the vector network analyzer (VNA, Keysight, P5002A) is amplified by a microwave amplifier (MA) and then fed into the EOM to intensity-modulate the dual-wavelength laser (carrier signal). The modulated optical signal passes through a dispersive delay line (dispersion coefficient of –168 ps/nm @1545 nm) and is then directed into a photodetector (PD, Shenzhen HLT Optical Technology Co., Ltd.), where it is converted from an optical signal to an RF signal. Finally, port 2 of the VNA receives the signal, obtains the RF domain interference spectrum, and displays it on the computer.

Filters in the laser cavity and dual-wavelength laser output

The filter in Path 1 inside the laser cavity employs a tapered lasso-shaped fiber sensor, which consists of alternately spliced single-mode fiber (SMF) and coreless fiber (CLF). As shown in Fig. 2(a), the SMF is first spliced with a small segment of CLF about 1 mm long, followed by a small segment of SMF about 8 mm long, then another small segment of CLF about 1 mm long, and finally, an SMF is used for the signal output. The middle SMF section is heated by hydrogen-oxygen flame and stretched to form a tapered optical fiber with a minimum diameter of 14.4 μm. The optical fiber is bent to get a lasso structure. A glass capillary tube with an inner diameter of 0.9 mm is attached to maintain the lasso structure and UV curing adhesive is injected into the glass tube to enhance the structural stability.

The tapered lasso-shaped fiber sensor is a multimode interferometer[19]. The arrow on the structural diagram in Fig. 2(a) briefly describes the transmission direction of the optical signal within the structure. Through simulation with RSOFT software, Fig. 2(b) presents the optical field energy distribution inside the sensing probe and tapered region of structure, visually demonstrating the optical transmission path and interference phenomena. The parameters set in the simulation are as follows: The free-space optical wavelength is set to 1.55 μm. The core and cladding diameters of the SMF are 8.2 μm and 125 μm, respectively. The cladding diameter of the CLF is 125 μm. The cladding diameter of the tapered section is set to 15 μm, and the core diameter is set to scale down proportionally. The RI of the core and cladding of SMF are 1.457 and 1.4447, respectively. The RI of the CLF is 1.4447. Simulation results show that when light from the SMF core passes through the CLF, the beam diffuses and propagates forward simultaneously in both core and

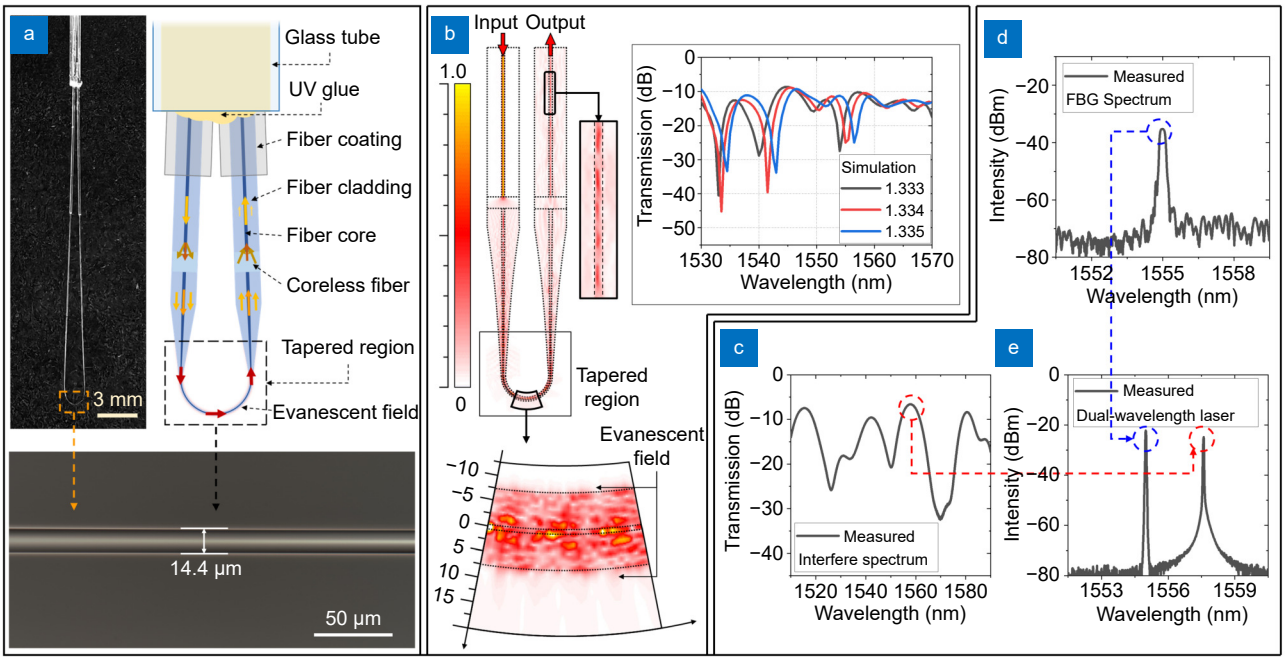

Fig. 2 | (**a**) Schematic diagram and detail enlarging diagram of the tapered lasso-shaped fiber sensor. (**b**) Simulation results of the light field energy distribution in the sensing probe, tapered region (locally enlarged) and output SMF section (locally enlarged), as well as simulated transmission spectrum of output signal. (**c**) Interference spectrum of tapered lasso-shaped fiber sensor. (**d**) Reflection spectrum of FBG. (**e**) Dual-wavelength laser spectrum.

cladding modes. In the tapered lasso region, the cladding mode generates much evanescent field energy on the cladding surface, which interacts with the surrounding environment, as shown in the electromagnetic field distribution diagram in Fig. 2(b). Compared with the original straight structure, the bending design to form a lasso structure allows more evanescent field to interact with the external environment (see detailed comparison in Supplementary information Fig. S1).

At the second segment of CLF (serving as a beam combiner), the core and cladding modes meet and enter the core of the subsequent SMF together. Since the core and cladding modes travel through different paths before merging, a phase difference arises, leading to an interference phenomenon. Simulation results at the output SMF region (after second segment of CLF, locally enlarged) shows that there are confined modes in the fiber core. The periodic changes of red color and light pink are shown in the electromagnetic field distribution diagram, indicating a periodic intensity change. The spectral analysis of the simulated output signal is also given in Fig. 2(b), which verifies the existence of interference phenomena of the output signal. When the surrounding RI of the sensor is changed, set to be 1.333, 1.334 and 1.335 respectively, the simulated transmission spectrum will redshift due to the evanescent field's perception of the surrounding environment. When the ambient RI increases, due to the interaction between the evanescent field and the surrounding environment, the effective RI of micro-fiber becomes larger (see Supplementary information Fig. S2), thus making the overall optical path of the sensor larger. Therefore, the resonant wavelength of the interference also increases synchronously, resulting in the spectrum redshift with the increase of the ambient RI. Figure 2(c) shows the experimental measured interference spectrum of the tapered lasso-shaped fiber sensor. Due to the slight deviation between the simulation parameters and actual situation, there are differences between the measured spectra and the simulated output power spectra, but the overall characteristics are similar, exhibiting distinct interference characteristics.

In Path 2, filtering is achieved using an FBG. The reflection wavelength of the FBG used is approximately 1555 nm, as shown in Fig. 2(d). To enhance the stability of the FBG, a glass capillary tube with an inner diameter of 0.5 mm and UV-curing glue is used to reinforce it, leaving only the sensing area of the FBG exposed at the end face. Although the filtering effects of the two filters in Path 1 and Path 2 are independent, they can be fixed together on the same glass slide for simultaneous

detection, as shown in the inset of Fig. 1, which ensures that the sensing areas of both are highly aligned and can be simultaneously immersed in the sample under test to sense environmental changes. Under the combined effect of the filtering by the FBG (indicated by the blue dashed line) and the interference filtering of the tapered lasso-shaped fiber sensor (indicated by the red dashed line), the final dual-wavelength laser spectrum is shown in Fig. 2(e). Laser signals with narrow linewidth, and a signal-to-noise ratio (SNR) exceeding 50 dB are formed near approximately 1555 nm and 1557.6 nm, respectively. The 3 dB bandwidths of the laser spectrum are both 0.04 nm.

Principle of microwave photonic demodulation

The principle of microwave photonics demodulation based on dispersion-induced time delay is shown in Fig. 3. The dual-wavelength laser signals, serving as carrier signals, are synchronously transmitted into the EOM and undergo intensity modulation by the RF signal. Subsequently, the two carriers with different laser wavelengths synchronously enter the dispersive delay line. Due to dispersion, light with different wavelengths travels at different speeds in the delay line, resulting in a transmission delay between the two carriers. Finally, when they reach the PD, the PD only senses the intensity variation of carrier signals (RF signal). Due to the time delay between the two carriers, the combine of RF signals produces interference phenomena, forming an interference spectrum in the frequency domain.

Set the dispersion coefficient and the transmission length of the dispersion delay line are D and L respectively, the two wavelengths of laser signals are $\lambda_{\rm ref}$ (laser-reference) and $\lambda_{\rm sensing}$ (Laser-sensing). The time delay Δt of the two carriers (laser signals) after the dispersion delay line can be expressed as:

$$\Delta t = DL\left(\lambda_{\rm sensing} - \lambda_{\rm ref}\right) \ . \tag{1}$$

If the frequency of the microwave signal is $f_{\rm RF}$, then the phase difference $\Delta\varphi_{\rm RF}$ of the modulated signal (caused by the time delay) perceived by the photodetector can be expressed as:

$$\Delta\varphi_{\rm RF} = 2\pi \times f_{\rm RF} \times \Delta t \ . \tag{2}$$

When the phase difference of the modulated signal (microwave signal) is accumulated to an odd multiple of π, the RF response of microwave photonic demodulation (interference signal) reaches the weakest point. The resonant valley frequency of the RF response spectrum can be expressed as:

$$\begin{aligned} f_{\text{RF-Dip}} &= (2k+1)/(2\Delta t) \\ &= (2k+1)/\left[2DL\left(\lambda_{\rm sensing} - \lambda_{\rm ref}\right)\right],\ k = 0,\ 1,\ 2,\ 3,\ \ldots \end{aligned} \tag{3}$$

The period of the interference spectrum of the RF response, i.e. the free spectral range (FSR), can be expressed as:

$$FSR_{\rm RF} = 1/\Delta t \ = 1/\ \left[DL\left(\lambda_{\rm sensing} - \lambda_{\rm ref}\right)\right] \ . \tag{4}$$

From Eq. (3) and Eq. (4), both the resonant valley frequency and the FSR of the RF interference spectrum are inversely proportional to the wavelength difference of

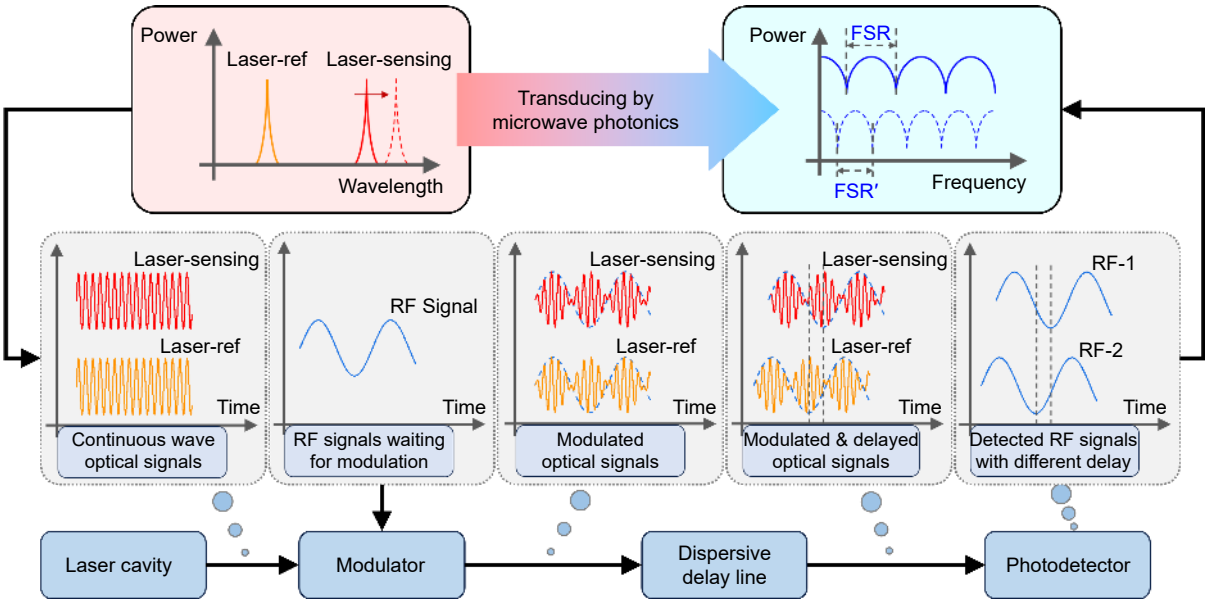

Fig. 3 | Principle of microwave photonic demodulation based on optical dispersion induced time delay.

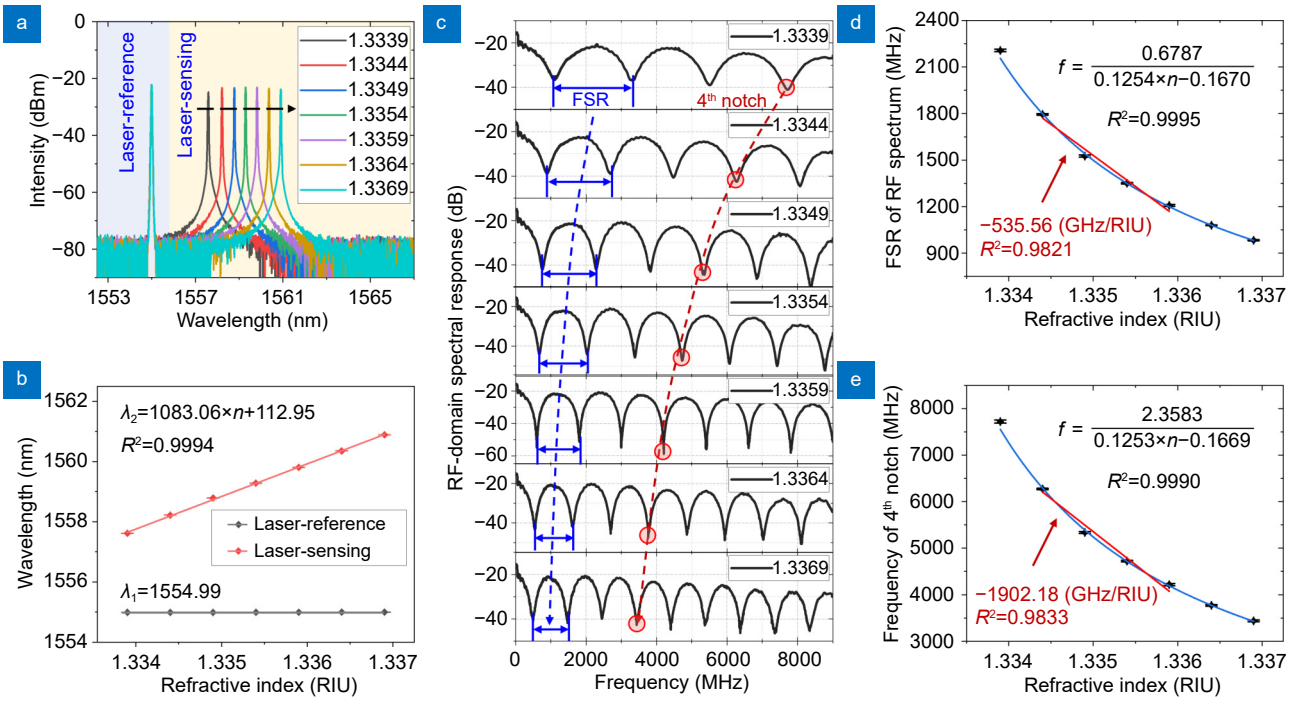

Fig. 4 | (**a**) Dual-wavelength laser spectra in solutions with different RIs. (**b**) fitting relationship between laser wavelength and RI. (**c**) RF spectrum in solutions with different RIs. (**d**) FSR response with RI and its fitting curve. (**e**) The 4th notch frequency response with RI and its fitting curve.

the dual-wavelength laser. When the wavelength difference changes, both the resonant valley frequency and the FSR will also change. Thus, variations in the laser wavelengths of the dual-wavelength laser spectrum are converted into frequency variation information in the RF spectrum.

Results and discussion

RI detection and wavelength-frequency dual-domain analysis

The FBG and the tapered lasso-shaped fiber sensor are simultaneously immersed in different NaCl solutions with RIs ranging from 1.3339 to 1.3369 to observe the spectral shifts, based on which the sensitivity response of the sensor to external RI variation is judged. In order to reduce the influence of factors such as ambient temperature change and vibration on the test results, during the entire RI test and subsequent biological detection experiment, the test was operated on an optical table, and the room temperature is controlled as much as possible (air conditioning temperature 20 °C). As shown in Fig. 4(a), with the increase of the external RI, the laser corresponding to FBG remained stable without any shift, which is consistent with previous studies that ordinary FBG is insensitive to external RI change. In contrast, the laser corresponding to the tapered lasso-shaped fiber sensor exhibits a red shift with increasing RI. Figure 4(b) shows the linear fitting relationship between the laser wavelengths and RI. The laser wavelength corresponding to FBG stabilizes at 1554.99 nm (reference laser); while the laser wavelength corresponding to the tapered lasso-shaped fiber sensor increases linearly with the RI (sensing laser), and its sensitivity is 1083.06 nm/RIU, with a linearity of 0.9994. Since the best resolution of the OSA used is 0.02 nm, the theoretical RI detection resolution based on laser spectral analysis can be calculated to be 1.85×10^{-5} RIU. However, the actual resolution will be limited by the performance of the sensor itself. Considering the maximum standard deviation σ of the wavelength shift fluctuation for multiple measurements (5 times for each solution) is 0.023 nm, the real detection accuracy is 2.12×10^{-5} RIU.

The smaller taper diameter, as well as the smaller bending diameter, help to improve the response sensitivity of the effective RI of the micro-fiber to the external RI variation (see Supplementary information Fig. S3), which helps to increase the fiber sensor's sensitivity. The tapered fiber with smaller diameter has a larger spectral response sensitivity. More experimental results can be found in Supplementary information Fig. S4. Considering that the robust structure and stable performance of

the sensor are crucial when measuring in complex environments or viscous liquids (such as body fluids). Here, the tapered lasso-shaped fiber sensor with taper diameter of 14.4 μm and bending diameter of around 2 mm are used for subsequent biosensing performance verification. Moreover, the fixing of the glass sleeve to the structure, the stretching and extrusion of the material by the bending of the optical fiber, and the stress balance of the structure itself ensure the stability of the sensor structure. The weak force of the sensor during repeated immersion in the liquid is not enough to affect the lasso structure, which ensures that the detection results of the sensor in the repeated detection process are reliable. This has been confirmed by our previous experimental results[19].

The RI detection analysis based on microwave photonics demodulation is carried out simultaneously. Figure 4(c) shows the RF interference spectra in different RI environments. As the RI increases, the RF spectrum becoming tighter, and the frequency of the FSR and each resonant valley point (or called notch) decreases accordingly. Figure 4(d) depicts the relationship between FSR and external RI and its fitting curve. According to Eq. (4), when the parameter of the dispersion delay line is constant, FSR is inversely proportional to the laser wavelength difference. Because the laser wavelength difference is linear to the external RI according to the fitting result in Fig. 4(b), FSR and the external RI should be inversely proportional. Using inverse proportional function fitting (represented by the blue solid line), the functional relationship between FSR and the external RI can be obtained as follows:

$$FSR_{\mathrm{RF}} = 0.6787/\left(0.1254 \times n - 0.1670\right), \tag{5}$$

with a good fitting degree of R^2=0.9995. In the application of biological detection, the RI of the dissolved biomolecular solution diluted by PBS buffer basically around 1.335. To simplify the operation, linear fitting is performed in the smaller RI range of 1.3344–1.3359, and the sensitivity of −535.56 GHz/RIU is obtained by linear fitting (solid red line) with a good fitting degree of R^2=0.9821. The RF spectrum resolution is set to 0.1 MHz, the theoretical detection resolution is 1.87×10^{-7} RIU. However, the maximum standard deviation σ of the frequency fluctuation for multiple measurements (5 times for each solution) is around 3.4 MHz. Thus, the real measurement accuracy is 6.35×10^{-6} RIU.

The period of the RF spectrum becomes denser as the RI increases, and the frequency of each notch decreases. To maximize the offset effect of spectrum, the maximum notch frequency is selected as the reference point of the sensing signal. When the RI of solution is 1.3339, the RF spectrum contains only 4 notches due to the large FSR. Therefore, the 4th notch is the largest notch that can be selected during this entire RI test process. The frequency of the 4th notch, is taken as the reference point of the sensing signal, marked by the red circle in Fig. 4(c). The relationship between the frequency of the 4th notch and the RI is shown in Fig. 4(e). Similarly, an inverse proportional function (blue fitting line) can be obtained:

$$f = 2.3583/\left(0.1253 \times n - 0.1669\right), \tag{6}$$

with a fitting degree of R^2=0.9990. The data in the RI range of 1.3344–1.3359 are linearly fitted (red solid line), and the sensitivity of −1902.18 GHz/RIU is obtained. The coefficient R^2=0.9833, indicating that the fitting effect is good. The resolution of RF spectrum is 0.1 MHz, and the theoretical RI detection resolution can be calculated as 5.26×10^{-8} RIU. Considering the maximum standard deviation σ of the 4th notch shift fluctuation for multiple measurements (5 times for each solution) is around 15.1 MHz, corresponding to a real measurement accuracy of 7.94×10^{-6} RIU.

In Table 1, the RI detection performances of our sensing system based on wavelength domain and frequency domain analysis are listed and compared with that of other optical fiber sensors reported in recent years.

As evident from Table 1, the sensing system proposed in this paper, utilizing microwave photonic demodulation for RF spectrum analysis within the same structure, significantly enhances the theoretical RI detection resolution and real detection accuracy compared to traditional spectral wavelength variation analysis, achieving a performance improvement of one and even two orders of magnitude. When compared to other recently published optical fiber sensing technologies, including those based on spectral wavelength shift, light intensity variation, speckle analysis, and microwave photonic demodulation, our proposed sensing system demonstrates higher sensitivity, superior resolution and better real detection accuracy in RI detection.

Antibody functionalization

Using the tumor marker Carcinoembryonic antigen-related cell adhesion molecule 5 (CEACAM5) as the specific detection target, the sensor is modified with anti-CEA-

Table 1 | The RI detection performance and comparison of optical fiber sensors proposed in recent years.

Sensors and demodulation method	RI detection sensitivity	Theoretical detection resolution (RIU)	Maximum σ during multiple measurements	Real detection accuracy b2(RIU)	Reference (Year)
Graphene-assisted D-shaped PCF sensor, wavelength shift	7,500 nm/RIU	1.33×10^{-5}	Not found	Not found	ref.[26] (2022)
Gold-coated hollow-core fiber, wavelength shift	6,000 nm/RIU	2.50×10^{-5}	Not found	Not found	ref.[27] (2023)
D-shaped PCF-based SPR sensor, wavelength shift	12,100 nm/RIU	8.26×10^{-6}	Not found	Not found	ref.[28] (2024)
Hollow core PCF-based SPR sensor, wavelength shift	9,217.22 nm/RIU	1.09×10^{-5}	Not found	Not found	ref.[29] (2023)
Random Raman fiber laser sensor, light intensity variation	–39.88 W/RIU	2.51×10^{-5}	0.012 W	3.0×10^{-4}	ref.[30] (2023)
Tapered multimode fiber, speckle analysis	19.52 /RIU	5.84×10^{-5}	0.0012	6.15×10^{-5}	ref.[31] (2023)
Au-coated TFBG fiber sensor, time-domain microwave photonics demodulation	–213 μs/RIU	7.50×10^{-7}	15.2 ns	7.13×10^{-5}	ref.[32] (2022)
MZI fiber sensor, frequency-domain microwave photonics demodulation	–1.11 GHz/RIU	9.00×10^{-7}	< 0.1 MHz	$< 9.00\times10^{-5}$	ref.[33] (2022)
Dual-wavelength fiber laser, wavelength shift	1083.06 nm/RIU	1.85×10^{-5}	0.023 nm	2.12×10^{-5}	In this paper
Frequency domain microwave photonics demodulation, FSR variation	−535.56 GHz/RIU	1.87×10^{-7}	3.4 MHz	6.35×10^{-6}	In this paper
Frequency domain microwave photonics demodulation, maximal notch frequency shift	−1902.18 GHz/RIU	5.26×10^{-8}	15.1 MHz	7.94×10^{-6}	In this paper

CAM5 antibodies. Figure 5(a) illustrates the flowchart of the antibody functionalization process. The antibody modification steps are as follows: Firstly, the optical fiber is immersed in freshly prepared piranha solution for 60 minutes to generate the hydroxyl functional groups on the surface of the fiber. Subsequently, the treated optical fiber is cleaned with deionized water and anhydrous ethanol, and then immersed in a 5% APTES ethanol solution for 90 minutes to aminate its surface. After that, the optical fiber is cleaned again and immersed in a 5% glutaraldehyde PBS solution for 45 minutes to produce aldehyde groups on the surface. Next, after cleaning the optical fiber with fresh PBS buffer, it is immersed in the anti-CEACAM5 antibody solution (concentration of 50 μg/mL) for 60 minutes to achieve antibody immobilization. Finally, the optical fiber is soaked in a BSA-TBS blocking solution for 30 minutes to block unbound aldehyde sites.

To verify the success of antibody modification, anti-CEACAM5 antibodies labeled with fluorescein isothiocyanate (FITC) are used, followed by fluorescence microscopy imaging. FITC is an organic fluorescent dye that can absorb blue light at 490–495 nm and emit green light at 525–530 nm. It is commonly used for covalent attachment to target molecules for visualization, detection, and quantification. The antibodies labeled with FITC are modified according to the process shown in Fig. 5(a). After washing steps in PBS buffer to remove unbound biomolecules, the antibody-bound optical fiber and an unmodified optical fiber are placed under an inverted fluorescence microscope (model XD-RFL, SOPTOP) for observation. As shown in Fig. 5(b), there is no significant difference between the two fibers under dark conditions. However, when illuminated with blue light at 490-495 nm, as shown in Fig. 5(c), the surface of the optical fiber modified with FITC-labeled antibodies emitted green fluorescence, while the unmodified fiber showed no fluorescent signal. This stark contrast visually demonstrates the successful modification of antibody on the optical fiber surface, indicating a stable binding effect.

Tumor marker detection in PBS buffer

CEACAM5 protein molecules are used as specific detection targets. The lyophilized powder of CEACAM5 is fully dissolved and homogenized in PBS buffer and diluted to different concentrations: 0.2 ng/mL, 0.4 ng/mL, 1 ng/mL, 2 ng/mL, 4 ng/mL, 10 ng/mL, 40 ng/mL, 100 ng/mL, and 400 ng/mL. The prepared CEACAM5 solutions of various concentrations are stored at 4 °C for short-term refrigeration. Pure PBS buffer is used as a blank control group.

The antibody-modified optical fiber biosensor is firstly

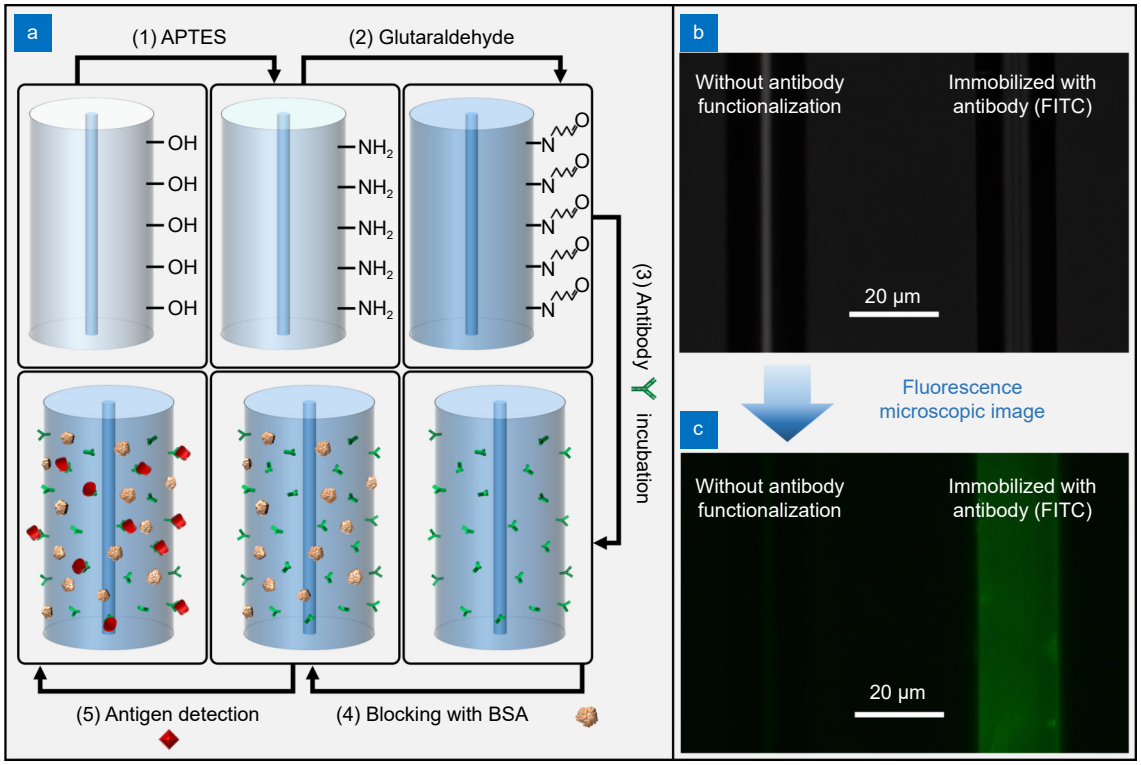

Fig. 5 | (**a**) Flow diagram of antibody modification on the fiber surface for antigen detection. (**b**) Microscopic imaging in a low light environment, and (**c**) fluorescence microscopic imaging of optical fiber sensors without antibody functionalization and immobilized with antibody (FITC labeled).

soaked in a PBS buffer for 15 minutes to remove the unstable binding biomolecules. Then the blank control group is tested. Figure 6(a) shows the dual-wavelength laser spectrum during the test of the blank control group. The continuous 40-minute monitoring of the reference laser wavelength (blue dot and line) and the sensing laser wavelength (red dot and line) during the testing are shown in Fig. 6(b). During this period, the wavelength of the reference laser and the sensing laser is stable, the maximum offset of the laser wavelength difference is 0.01 nm, the average wavelength change $\overline{\Delta(\lambda_{\rm sens}-\lambda_{\rm ref})_{\rm blank}}$ is 0.002 nm, and the standard deviation σ of the random fluctuation is 0.008 nm. RF spectrum information based on microwave photonics demodulation is also recorded synchronously, and Fig. 6(c) shows the RF spectrum during the test of the blank control group. Continuous monitoring of spectral FSR changes and the maximum notch ($5^{\rm th}$ notch) frequency changes within 40 mins is shown in Fig. 6(d). The FSR is relatively stable, with a random fluctuation standard deviation σ of 2.3 MHz and an average variation $\overline{(\Delta FSR_{\rm RF})_{\rm blank}}$ of 2.0 MHz. The random fluctuation of the frequency change of the $5^{\rm th}$ notch is slightly larger, with an average change $\overline{(\Delta f_{5-{\rm notch}})_{\rm blank}}$ of 9.9 MHz and a standard deviation σ of 12.9 MHz.

The sensor is immersed in CEACAM5 solution of different concentrations for 40 mins to fully react and then immersed in PBS buffer 3 times to remove the unstably bound biomolecules, and then record dual-wavelength laser spectra, as shown in Fig. 7(a). Compared with the laser spectrum in PBS, the laser spectrum after reaction with CEACAM5 solution has an observable change. The specific performance is that the wavelength of the reference laser remains unchanged, and the wavelength of the sensing laser becomes larger. Moreover, the wavelength variation of the sensing laser is positively correlated with the concentration of CEACAM5 solution. Therefore, the change in the laser wavelength difference is positively related to the concentration of the CEACAM5 solution. The change in the laser wavelength difference corresponds to the concentration of the CEACAM5 solution is shown in Fig. 7(b). The concentration of the CEACAM5 solution has a significant influence on the sensor detection results. When the concentration is less than 1 ng/mL, due to the limitations of sensitivity and demodulation resolution, the sensor's response to the concentration change is not obvious. As the concentration increases, the sensor begins to sensitively detect the difference in molecular concentration. However, when the concentration rises to

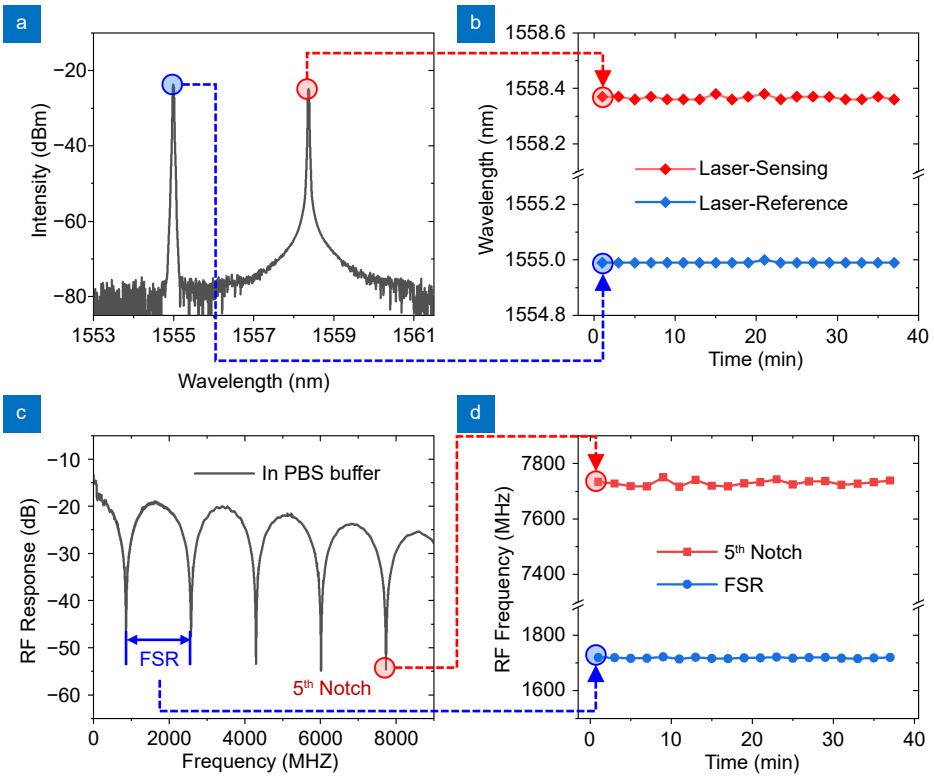

Fig. 6 | (**a**) Dual-wavelength laser spectrum during blank control test. (**b**) Continuous monitoring of laser wavelengths during blank control test. (**c**) RF spectrum based on microwave photonics demodulation during blank control test. (**d**) Continuous monitoring of FSR and the 5th notch frequency during blank control test.

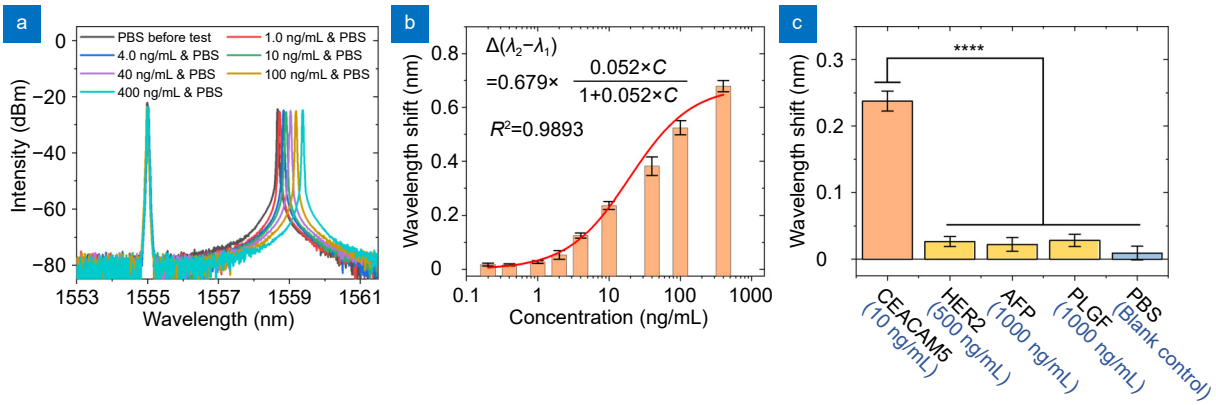

Fig. 7 | (**a**) Dual-wavelength laser spectra after sufficient reaction in CEACAM5 solutions with different concentrations. (**b**) The fitting relationship between the change in wavelength difference and CEACAM5 concentration. (**c**) Comparison and significance difference test of the variation of laser wavelength difference between CEACAM5 solution, non-specific protein control groups and blank control group.

a certain extent, the antigen-antibody binding sites on the sensor surface tend to be saturated, resulting in a slowdown in response increase. Langmuir isotherm equation[34,35] can be used to fit the above change trend, and the formula can be expressed as:

$$\Delta\left(\lambda_{\rm sens}-\lambda_{\rm ref}\right)=\left[\Delta\left(\lambda_{\rm sens}-\lambda_{\rm ref}\right)\right]_{\rm max}\times\left[KC/\left(1+KC\right)\right]\ , \tag{7}$$

where C is the biomolecular concentration (ng/mL) and K is the equilibrium binding constant, which describes the ratio between unbound and bound antibodies under steady-state conditions. The detection results of each concentration in Fig. 7(b) are fitted according to Eq. (7), and the following relationship can be obtained:

$$\Delta\left(\lambda_{\rm sens}-\lambda_{\rm ref}\right)=0.679\times\left[\left(0.052\times C\right)/\left(1+0.052\times C\right)\right]\ . \tag{8}$$

The coefficient of determination R^2 = 0.9893, and the fitting effect is good. According to Eq. (8), the function relation with the change of laser wavelength difference

$\Delta(\lambda_{sens}-\lambda_{ref})$ as the independent variable and the concentration C as the dependent variable is obtained:

$$C=\Delta(\lambda_{sens}-\lambda_{ref})\,/\,\{[0.679-\Delta(\lambda_{sens}-\lambda_{ref})]\times 0.052\}. \tag{9}$$

The minimum signal that the sensing system can resolve is limited by blank control noise (σ) and the demodulation resolution of the device. Considering that the $\overline{\Delta(\lambda_{sens}-\lambda_{ref})_{blank}}+3\sigma$ (threshold to distinguish effective signal from random noise) of the sensor in the blank control group is 0.026 nm, the LOD based on spectral wavelength analysis can be calculated as 0.77 ng/mL according to Eq. (9). The LOD calculated by the formula is in good agreement with the experimental results obtained by OSA measurement.

To validate the specificity of our designed biosensor, three sets of nonspecific protein control groups are set, that are 500 ng/mL human epidermal growth factor receptor 2 (HER2) solution, 1000 ng/mL alpha-fetoprotein (AFP) solution, and 1000 ng/mL placental growth factor (PLGF) solution. HER2 serves as a vital marker for various tumors such as breast cancer and ovarian cancer, AFP is primarily associated with liver cancer, and PLGF is expressed in multiple tissues, closely related to angiogenesis. In each testing of nonspecific protein control groups, the sensor is immersed in the solution for 40 minutes, followed by thorough rinsing in PBS buffer, while wavelength changes are recorded. After sufficient reaction and rinsing processes, the spectral differences before and after the experiments are compared. The results show that the laser difference changes in HER2, AFP and PLGF control groups were 0.027 nm, 0.023 nm, and 0.028 nm, respectively. Comparing the experimental results of all groups, the signal responses of the non-specific protein control group and blank control group are the same order of magnitude, and significantly lower than that of the CEACAM5 solution. Specifically, a 10 ng/mL solution of CEACAM5 as a specific target causes a wavelength shift of 0.238 nm, nearly 10 times that of non-specific proteins with higher concentrations. The significant difference ($p < 0.0001$) is confirmed by statistical tests, indicating that the sensor has a highly specific ability to detect CEACAM5.

The change of laser wavelength caused by biological immune binding in the CEACAM5 solution also synchronously causes the signal change in the RF spectrum, as shown in Fig. 8(a). Compared with the RF spectrum in PBS buffer, the RF spectrum after reaction in CEACAM5

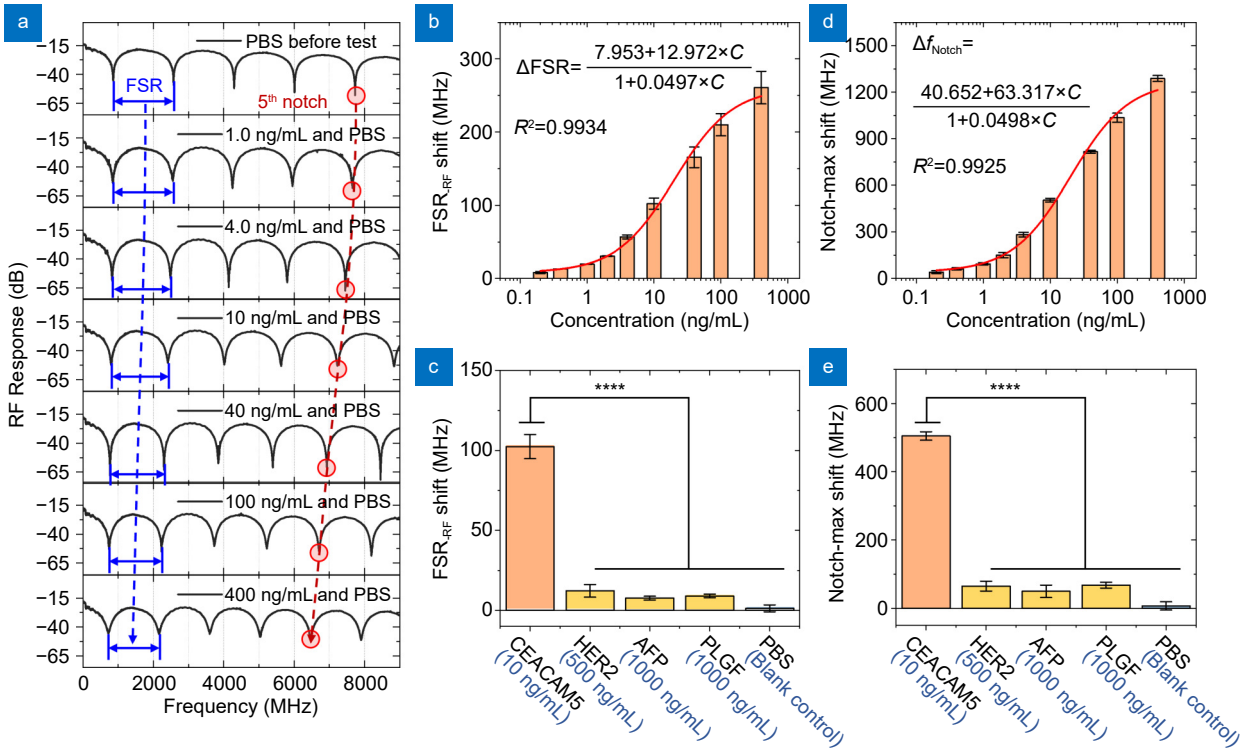

Fig. 8 | (**a**) RF spectra based on microwave photonic demodulation after sufficient reaction in CEACAM5 solution with different concentrations. (**b**) The fitting relationship between spectral FSR reduction and CEACAM5 concentration. (**c**) Comparison of spectral FSR reduction in different control groups and their significance difference test. (**d**) The fitting relationship between 5th notch frequency reduction and CEACAM5 concentration. (**e**) Comparison of 5th notch frequency in different control groups and their significance difference test.

solutions becomes denser. In Fig. 8(a), the blue dashed line marks the decreasing trend of FSR, and the red dashed line marks the decreasing trend of the 5th notch frequency. These frequency changes are positively correlated with CEACAM5 solution concentration. With the increase in concentration, the decrease in frequency is greater.

Figure 8(b) visually shows the relationship between FSR and CEACAM5 concentration. With the increase of concentration, the frequency of FSR decreases first slowly, then quickly, and finally slowly. This trend is fitted by the Langmuir isotherm model, and the corresponding relation is obtained:

$$|\Delta FSR_{\rm RF}| = (7.953 + 12.972 \times C) \,/\, (1 + 0.0497 \times C) \ . \tag{10}$$

The coefficient of determination R^2 = 0.9934, indicating that the fitting effect is good. According to Eq. (10), a relationship that takes the reduction of FSR as the independent variable and concentration C as the dependent variable can be obtained:

$$C = (|\Delta FSR_{\rm RF}| - 7.953) \,/\, (12.972 - 0.0497 \times |\Delta FSR_{\rm RF}|) \ . \tag{11}$$

Considering that the $\overline{(\Delta FSR_{\rm RF})_{\rm blank}} + 3\sigma$ of the sensor in the blank control group (the threshold that distinguishes the effective signal from random noise) is 8.9 MHz, substituting it into Eq. (11), the LOD based on the FSR variation can be obtained as 0.076 ng/mL. The resolution of RF spectrum used here is 0.1 MHz, and the detection resolution between LOD can be calculated as 0.008 ng/mL.

The sensors are fully reacted in different nonspecific protein control groups and blank control groups, and after soaking in the new PBS buffer, the reduction of spectral FSR (compared with the value soaked in PBS buffer before the reaction) is recorded and compared in Fig. 8(c). There are significant differences between the CEACAM5 solution and other nonspecific protein control groups with higher concentrations. In 500 ng/mL HER2 solution, 1000 ng/mL AFP solution, and 1000 ng/mL PLGF solution, the FSR reduction is 12.29 MHz, 7.69 MHz, and 9.05 MHz, respectively, which is slightly higher than 2 MHz in the blank control group. However, in CEACAM5 solutions with concentrations as low as 10 ng/mL, the reduction of FSR reaches 102.37 MHz, which is an order of magnitude greater than that in the nonspecific protein control groups. This shows that even if the concentration of nonspecific protein is 100 times greater than CEACAM5, their disturbance with CEACAM5 detection is still small. The variation of spectral FSR in these control tests is tested for significant differences. In Fig. 8(c), **** represents a hypothesis test with p < 0.0001, which further confirms that there are significant differences between CEACAM5 and other nonspecific proteins as well as the blank control group. These results fully demonstrate the specific detection ability of the sensor for CEACAM5.

It can be seen from the microwave photonic demodulated RF spectrum that the maximum notch (5th notch) frequency variation is much larger than the spectral FSR variation. Figure 8(d) shows the relationship between 5th-notch frequency reduction and concentration of CEACAM5. Langmuir isotherm model is used to fit the change trend:

$$\Delta f_{5-\rm notch} = (40.652 + 63.317 \times C) / (1 + 0.0498 \times C) \ , \tag{12}$$

The coefficient of determination R^2 = 0.9925 indicates that the fitting effect is good. According to Eq. (12), a functional relation with the frequency reduction of 5th notch as the independent variable and concentration C as the dependent variable is obtained:

$$C = (\Delta f_{5-\rm notch} - 40.652) / (63.317 - 0.0498 \times \Delta f_{5-\rm notch}) \ , \tag{13}$$

According to the $\overline{(\Delta f_{5-\rm notch})_{\rm blank}} + 3\sigma$ in the blank control group (the threshold to distinguish effective signal from random noise) is 48.6 MHz, the LOD based on the analysis of 5th notch frequency reduction is 0.131 ng/mL.

The 5th notch frequency reduction in CEACAM5 solution, nonspecific protein control groups, and blank control groups are compared in Fig. 8(e), which presents a stark contrast. The 5th notch frequency decrement caused by reactions in HER2 solution, AFP solution, and PLGF solution is 65.21 MHz, 50.18 MHz, and 68.06 MHz, respectively. In contrast, the decrease in the 5th notch frequency in the CEACAM5 solution at a concentration as low as 10 ng/mL is 505.07 MHz, which is an order of magnitude higher than that in those nonspecific protein control groups. Even with a 100-fold advantage in concentration, higher concentrations of nonspecific protein molecules have less interference with the detection of lower concentrations of CEACAM5 molecules. Meanwhile, a significant difference test is conducted in these specificity validation experiments. In Fig. 8(e), **** indicates a hypothesis test with p < 0.0001, suggesting a significant difference between the CEACAM5 solution and

the other three nonspecific protein solutions, as well as the blank control group. These results fully demonstrate the good specificity of the sensor for detecting CEACAM5.

As shown in Table 2, the biosensing performance of the three analysis methods mentioned above is summarized and compared. Compared with the laser wavelength variation analysis, the microwave photonics demodulation-based RF spectrum analysis performs better in biological detection, achieving an order of magnitude improvement in detection performance. In RF spectrum analysis, although the maximum notch frequency reduction analysis shows higher sensitivity in RI detection, single notch frequency analysis may be affected by environmental vibration, transient jump of current and other factors, resulting in spectral burrs and fluctuations of single notch frequency. Thus, a larger frequency deviation is introduced during the test in blank control group, which affects the stability performance and limits the improvement of the detection performance. In contrast, FSR decrement analysis is more stable and exhibits better detection performance.

Table 2 also lists recently published works to detect CEACAM5 and the LODs of various biosensors are compared. The investigation includes optical biosensors based on fluorescence detection, surface-enhanced Raman scattering (SERS), as well as electrochemical biosensors, electrochemiluminescence biosensors, micro-electromechanical systems (MEMS) sensing technology. Our dual-wavelength laser sensing system enhanced with microwave photonics demodulation technology, effectively improves the detection performance, and achieves better LOD than many published works.

Tumor marker detection in serum samples

Using human serum samples to verify the clinical detection capability of the proposed sensing system. The human serum samples are obtained from Guangdong Provincial people's hospital (Guangzhou, China). Clinical processes have been approved by the Ethics Committees of Guangdong Provincial People's Hospital (KY-Q-2022-388-01). Prior to testing, the serum samples are removed from the refrigerator to thaw and evenly divided into 3–4 portions (0.4 mL each) for multiple independent tests. To ensure the accuracy of the tests, the samples to be tested has been stabilized at room temperature in advance to avoid the interference of temperature changes on the test results.

The measurement steps are as follows: Firstly, the sensor is immersed in a fresh PBS buffer to record initial spectrum information. Subsequently, the sensor is immersed in the serum sample to fully react and monitor

Table 2 | Performance comparison of different types of biosensors for CEACAM5 detection.

Types	Methods	Characteristic	LOD (ng/mL)	Reference (year)
Optical sensor	SERS, sensitized with gold nanoparticle (sandwich)	Low uniformity on SERS chip	0.258	Ref.[9] (2022)
Optical sensor	Microfiber sensitized by nano polystyrene@Au sphere	Unstable properties of self-assembly nanomaterials	0.08	Ref.[16] (2021)
Optical sensor	UV absorption of DNA/MoS2 nanosheets	Low sensitivity	50.0	Ref.[7] (2020)
Optical sensor	Fluorescence of the quantum dots on plasmonic arrays	Low sensitivity, affected by ambient light	5090	Ref.[36] (2022)
Optical sensor	Color of the solution changes (colorimetry)	Low sensitivity	24.8	Ref.[37] (2022)
Micro-electromechanical systems (MEMS) sensor	Monitor microcantilever bending	Susceptible to vibration	1.30	Ref.[38] (2019)
Electrochemiluminescence sensor	Multi-walled carbon nanotubes and nano-gold	Narrow response range	0.76	Ref.[39] (2022)
Electrochemical sensor	Electrochemical impedance spectroscopy	Low SNR	3.00	Ref.[40] (2019)
Optical sensor	Dual-wavelength fiber laser, wavelength shift	Robust sensing performance	0.77	In this paper
Optical sensor	Frequency domain microwave photonics demodulation, maximal notch frequency shift	The new demodulation method improves the detection performance	0.131	In this paper
Optical sensor	Frequency domain microwave photonics demodulation, FSR variation	The new demodulation method improves the detection performance	0.076	In this paper

signal changes. After a sufficient reaction in serum samples (spectral information stabilized), the sensor is removed, and rinse three times in a new PBS buffer to remove unstably bound biomolecules and minimize non-specific adsorption. Finally, the sensor is immersed in the initial PBS buffer again to record spectral information after the serum sample testing. By comparing the spectral information before and after the reaction, the laser wavelength shift, FSR reduction, and the maximum notch frequency reduction are analyzed. Previous experimental studies have shown that the antigen-antibody binding on the sensor surface is relatively stable[41,42]. Therefore, the rapid transfer from serum to PBS buffer does not affect this specific binding while the non-specific binding is removed, and the spectral changes reflect the true information of the serum sample. In addition, since all spectral information is obtained in the PBS buffer, the influence of RI differences between serum samples on the detection results is effectively avoided.

Figure 9 shows the detection results of tumor marker concentration in different serum samples by three experimental analysis and the comparison with the data provided by the hospital. The three experimental analysis methods can distinguish the concentration difference in serum samples, showing a similar trend with clinical data.

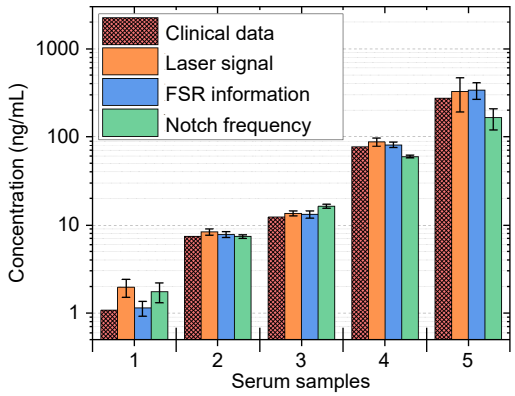

Fig. 9 | The testing results of serum samples based on three analysis methods and compared with the clinical data.

Table 3, Table 4 and Table 5 respectively show the deviation of laser wavelength difference, FSR reduction and maximum notch frequency reduction after measurement of each serum sample. The concentration of CEACAM5 in human serum is derived according to Eq. (9), Eq. (11), and Eq. (13) and compared with the clinical data. To quantitatively describe the difference between the two, the relative standard deviation (RSD) between the experimentally measured concentration and the clinical data is defined as:

$$RSD = |C_{\text{measured}} - C_{\text{clinical}}| / C_{\text{clinical}} \times 100\% \,. \tag{14}$$

The analysis method based on the laser wavelength difference variation is limited by the demodulation resolution and the sensitivity when testing the low-concentration samples (such as Sample 1), resulting in larger detection deviations, but the experimental results still conform to the actual situation. As the concentration increases, the detection results become more consistent with clinical values.

In serum samples with concentrations ranging from 1 to 100 ng/mL, the detection results of RF spectral FSR reduction analysis are consistent with expectations. At ultra-high concentrations, however, the deviation increases. This is mainly due to the slightly larger deviation in fitting relationship Eq. (11) at high concentrations, as shown in Fig. 8. Still, the method can effectively indicate the amount of excess and act as an early warning, so slight deviations at high concentrations have limited impact on practical applications. In general, it has good detection performance.

On the other hand, while the maximum notch frequency reduction analysis exhibits higher detection sensitivity, it is susceptible to fluctuations in a single notch frequency and increasing detection deviations. Nonetheless, this method can still effectively distinguish differences in CEA concentration in serum.

In summary, the analysis of FSR reduction based on microwave photonics demodulated RF spectrum demonstrates a superior detection performance in biological detection.

Table 3 | Detection results of CEACAM5 concentration in serum samples based on laser wavelength difference analysis.

Serum sample serial number	The increment of laser wavelength difference (nm)	Experimental test concentration (ng/mL)	Clinical data (ng/mL)	RSD
Sample 1	0.063 ± 0.013	1.96 ± 0.44	1.09	79.50%
Sample 2	0.205 ± 0.012	8.33 ± 0.67	7.42	12.26%
Sample 3	0.281 ± 0.011	13.62 ± 0.91	12.29	10.80%
Sample 4	0.556 ± 0.011	87.79 ± 9.50	76.24	15.15%
Sample 5	0.638 ± 0.013	327.56 ± 137.27	273.65	19.70%

Table 4 | Detection results of CEACAM5 concentration in serum samples based on RF spectral FSR reduction analysis.

Serum sample serial number	Frequency reduction of RF spectral FSR (MHz)	Experimental test concentration (ng/mL)	Clinical data (ng/mL)	RSD
Sample 1	21.56 ± 2.54	1.14 ± 0.22	1.09	5.02%
Sample 2	78.33 ± 3.91	7.76 ± 0.60	7.42	4.61%
Sample 3	108.16 ± 5.64	13.23 ± 1.25	12.29	7.61%
Sample 4	210.63 ± 3.25	81.27 ± 6.46	76.24	6.60%
Sample 5	246.17 ± 3.40	338.24 ± 70.89	273.65	23.60%

Table 5 | Detection results of CEACAM5 concentration in serum samples based on maximum notch frequency reduction analysis.

Serum sample serial number	Frequency reduction of maximum notch (MHz)	Experimental test concentration (ng/mL)	Clinical data (ng/mL)	RSD
Sample 1	139.17 ± 23.10	1.75 ± 0.44	1.09	60.92%
Sample 2	370.47 ± 11.93	7.35 ± 0.36	7.42	0.88%
Sample 3	592.34 ± 15.53	16.33 ± 0.83	12.29	32.85%
Sample 4	960.92 ± 8.91	59.56 ± 2.27	76.24	21.88%
Sample 5	1131.56 ± 31.24	163.96 ± 44.16	273.65	40.08%

Conclusions

In this paper, a dual-wavelength fiber laser sensor combined with microwave photonics demodulation technology based on dispersive time delay is proposed to achieve high-resolution measurement of tumor markers in serum. A tapered lasso-shaped fiber sensor is designed and connected in parallel with FBG, constructing a sensor system to realize dual-wavelength laser signal output. In the experiment, laser wavelength analysis using an OSA and RF analysis based on microwave photonics demodulation are conducted simultaneously. The sensing system achieves a RI sensitivity of 1083 nm/RIU based on laser wavelength analysis. Using microwave photonics demodulation technology, a sensitivity of −1902 GHz/RIU is achieved, improving detection resolution and real detection accuracy by two orders of magnitude compared to traditional OSA spectral detection. To verify the biosensor performance of the sensor, CEACAM5 is selected as the target analyte. Test results in PBS buffer show that the sensor has a LOD as low as 0.076 ng/mL, improving performance by an order of magnitude compared to traditional laser spectral wavelength demodulation schemes, and achieves better LOD than many published works. Furthermore, testing on human serum samples validates the practical application performance of the sensing system. The experimental schemes can effectively distinguish differences in CEA content in serum and are consistent with clinical values provided by the hospital. In the demodulation scheme and system design, solving the cross-sensitivity problem will effectively improve the detection capability of the sensor system. In the microwave photonic filter system, multiple sensors can be connected in parallel to realize simultaneous measurement of multiple parameters and solve the cross-sensitivity problem[24], which is the next step in our future research. All in all, compared to traditional spectral wavelength demodulation methods, microwave photonics demodulation technology based on dispersive time delay significantly improves detection accuracy and resolution and opens new possibilities for a wider range of biosensing scenarios.

References

1. Sung H, Ferlay J, Siegel RL et al. Global cancer statistics 2020: GLOBOCAN estimates of incidence and mortality worldwide for 36 cancers in 185 countries. *CA Cancer J Clin* **71**, 209–249 (2021).
2. Crosby D, Bhatia S, Brindle KM et al. Early detection of cancer. *Science* **375**, eaay9040 (2022).
3. Ren J, Cai H, Li Y et al. Tumor markers for early detection of ovarian cancer. *Expert Rev Mol Diagn* **10**, 787–798 (2010).
4. Zhou JF, Fan X, Chen N et al. Identification of CEACAM5 as a biomarker for prewarning and prognosis in gastric cancer. *J Histochem Cytochem* **63**, 922–930 (2015).
5. Su DS, Chen PY, Chiu HC et al. Disease antigens detection by silicon nanowires with the efficiency optimization of their antibodies on a chip. *Biosens Bioelectron* **141**, 111209 (2019).
6. Zhang DS, Li WX, Ma ZF et al. Improved ELISA for tumor marker detection using electro-readout-mode based on label triggered degradation of methylene blue. *Biosens Bioelectron* **126**, 800–805 (2019).
7. Zhao LJ, Wang J, Su DD et al. The DNA controllable peroxidase mimetic activity of MoS_2 nanosheets for constructing a robust colorimetric biosensor. *Nanoscale* **12**, 19420–19428 (2020).

8. Filik H, Avan AA. Electrochemical and electrochemiluminescence dendrimer-based nanostructured immunosensors for tumor marker detection: a review. *Curr Med Chem* **28**, 3490–3513 (2021).
9. Wang TY, Zhu YZ, Weng SY et al. Optical biosensor based on SERS with signal calibration function for quantitative detection of carcinoembryonic antigen. *Biomed Opt Express* **13**, 5962–5970 (2022).
10. Liu JJ, Jalali M, Mahshid S et al. Are plasmonic optical biosensors ready for use in point-of-need applications. *Analyst* **145**, 364–384 (2020).
11. Socorro-Leránoz AB, Santano D, Del Villar I et al. Trends in the design of wavelength-based optical fibre biosensors (2008-2018). *Biosens Bioelectron: X* **1**, 100015 (2019).
12. Liang LL, Jin L, Ran Y et al. Fiber light-coupled optofluidic waveguide (FLOW) immunosensor for highly sensitive detection of p53 protein. *Anal Chem* **90**, 10851–10857 (2018).
13. Chen XY, Xu P, Lin WE et al. Label-free detection of breast cancer cells using a functionalized tilted fiber grating. *Biomed Opt Express* **13**, 2117–2129 (2022).
14. Zhang YX, Wu H, Wang H et al. Ultraminiature optical fiber-tip directly-printed plasmonic biosensors for label-free biodetection. *Biosens Bioelectron* **218**, 114761 (2022).
15. Esposito F, Sansone L, Srivastava A et al. Long period grating in double cladding fiber coated with graphene oxide as high-performance optical platform for biosensing. *Biosens Bioelectron* **172**, 112747 (2021).
16. Xiao AX, Huang YY, Zheng JY et al. An optical microfiber biosensor for CEACAM5 detection in serum: sensitization by a nanosphere interface. *ACS Appl Mater Interfaces* **12**, 1799–1805 (2020).
17. Bian SM, Shang M, Sawan M. Rapid biosensing SARS-CoV-2 antibodies in vaccinated healthy donors. *Biosens Bioelectron* **204**, 114054 (2022).
18. Sun LP, Huang Y, Huang TS et al. Optical microfiber reader for enzyme-linked immunosorbent assay. *Anal Chem* **91**, 14141–14148 (2019).
19. Hu J, He PP, Zhao F et al. Magnetic microspheres enhanced peanut structure cascaded lasso shaped fiber laser biosensor for cancer marker-CEACAM5 detection in serum. *Talanta* **271**, 125625 (2024).
20. Yang X, Gong CY, Zhang CL et al. Fiber optofluidic microlasers: structures, characteristics, and applications. *Laser Photon Rev* **16**, 2100171 (2022).
21. Hu J, Song EL, Liu YH et al. Fiber laser-based lasso-shaped biosensor for high precision detection of cancer biomarker-CEACAM5 in serum. *Biosensors* **13**, 674 (2023).
22. Capmany J, Novak D. Microwave photonics combines two worlds. *Nat Photonics* **1**, 319–330 (2007).
23. Yao JP. Microwave photonics. *J Lightwave Technol* **27**, 314–335 (2009).
24. Xiao DR, Wang GQ, Yu FH et al. Optical curvature sensor with high resolution based on in-line fiber Mach-Zehnder interferometer and microwave photonic filter. *Opt Express* **30**, 5402–5413 (2022).
25. Cao Y, Wang XD, Guo T et al. High-resolution and temperature-compensational HER2 antigen detection based on microwave photonic interrogation. *Sens Actuators B Chem* **245**, 583–589 (2017).
26. Pakarzadeh H, Sharif V, Vigneswaran D et al. Graphene-assisted tunable D-shaped photonic crystal fiber sensor in the visible and IR regions. *J Opt Soc Am B* **39**, 1490–1496 (2022).
27. Divya J, Selvendran S. Surface plasmon resonance-based gold-coated hollow-core negative curvature optical fiber sensor. *Biosensors* **13**, 148 (2023).
28. Wang SF, Shen T, Feng Y et al. D-type photonic crystal fiber refractive index sensor with ultra-high fabrication stability and ultra-wide detection range. *Opt Quantum Electron* **56**, 515 (2024).
29. Wang FM, Wei Y, Han YH. High sensitivity and wide range refractive index sensor based on surface plasmon resonance photonic crystal fiber. *Sensors* **23**, 6617 (2023).
30. Han B, Ma YX, Wu H et al. Random raman fiber laser as a liquid refractive index sensor. *Photonic Sens* **14**, 240121 (2024).
31. Guo PL, Liu HH, Zhou ZT et al. Spatially modulated fiber speckle for high-sensitivity refractive index sensing. *Sensors* **23**, 6814 (2023).
32. Wang GY, Liao BL, Cao Y et al. Microwave photonic interrogation of a high-speed and high-resolution multipoint refractive index sensor. *J Lightwave Technol* **40**, 1245–1251 (2022).
33. Zhang YF, Zhang AL, Wang JF et al. High-sensitivity and high-resolution RI sensor with ultrawide measurement range based on NCF with large offset splicing and MPF interrogation. *IEEE Sens J* **22**, 22707–22713 (2022).
34. Chen LH, Chan CC, Ni K et al. Label-free fiber-optic interferometric immunosensors based on waist-enlarged fusion taper. *Sens Actuators B Chem* **178**, 176–184 (2013).
35. Liu LH, Shan DD, Zhou XH et al. TriPleX™ waveguide-based fluorescence biosensor for multichannel environmental contaminants detection. *Biosens Bioelectron* **106**, 117–121 (2018).
36. Susu L, Vulpoi A, Astilean S et al. Portable plasmonic paper-based biosensor for simple and rapid indirect detection of CEACAM5 biomarker via metal-enhanced fluorescence. *Int J Mol Sci* **23**, 11982 (2022).
37. Li P, Li WQ, Xie ZH et al. A label-free and signal-amplifiable assay method for colorimetric detection of carcinoembryonic antigen. *Biotechnol Bioeng* **119**, 504–512 (2022).
38. Li C, Ma XX, Guan YX et al. Microcantilever array biosensor for simultaneous detection of carcinoembryonic antigens and α-fetoprotein based on real-time monitoring of the profile of cantilever. *ACS Sens* **4**, 3034–3041 (2019).
39. Wang RN, Huang Y, Chi YW. Gold nanoparticles-oxidized multi-walled carbon nanotubes as electrochemiluminescence immunosensors. *Analyst* **147**, 3096–3100 (2022).
40. Truta LAANA, Sales MGF. Carcinoembryonic antigen imprinting by electropolymerization on a common conductive glass support and its determination in serum samples. *Sens Actuators B Chem* **287**, 53–63 (2019).
41. Browning-Kelley ME, Wadu-Mesthrige K, Hari V et al. Atomic force microscopic study of specific antigen/antibody binding. *Langmuir* **13**, 343–350 (1997).
42. Chen L, Leng YK, Liu B et al. Ultrahigh-sensitivity label-free optical fiber biosensor based on a tapered singlemode-no core-singlemode coupler for *Staphylococcus aureus* detection. *Sens Actuators B Chem* **320**, 128283 (2020).

Acknowledgements

This work was supported in part by the Science and Technology Department of Guangdong Province (2021A0505080002), Department of Natural Resources of Guangdong Province (GDNRC [2022] No. 22), Science, Technology and Innovation Commission of Shenzhen Municipality

(20220815121807001), Hunan Provincial Natural Science Foundation of China (under Grant Nos. 2023JJ30209), Hunan Provincial Education Department Science Research Fund of China (under Grant Nos. 22B0862).

Author contributions

J. Hu fabricated the sensor, performed the simulations, conducted the measurements, analyzed the experimental results, and wrote the original draft of the paper. W. H. Lin, C. L. Xue, and F. Zhao participated in experiments, helped analyze experimental results, reviewed, and edited the draft. Y. Ran, P. P. He, Z. G. Yu and J. N. Chen conceived the theoretical analysis, provided guidance on biological functionalization modification, reviewed, and edited the draft. Y. Meng help provide test samples from hospital, reviewed, and edited the draft. L. Y. Shao, D. R. Xiao and P. P. Shum supervised the project, reviewed, and edited the draft.

Competing interests

The authors declare no competing financial interests.

Supplementary information

Supplementary information for this paper is available at https://doi.org/10.29026/oea.2024.240105